Sheffield Hallam University

Self-Assembly of Nanosheet Supported Fe-MOFs Heterocrystal as Reusable Catalyst for Boosting Advanced Oxidation Performance via Radical and Nonradical Pathways

ZHANG, Bofan, ZHANG, Liang, AKIYAMA, Kazuhiko, BINGHAM, Paul
<http://orcid.org/0000-0001-6017-0798>, ZHOU, Yingtang and KUBUKI, Shiro

Citation:

Copyright and re-use policy

Self-Assembly of Nanosheet Supported Fe-MOFs Heterocrystal as Reusable Catalyst for Boosting Advanced Oxidation Performance via Radical and Nonradical Pathways

Bofan Zhang[1, †, *], Liang Zhang[2, †], Kazuhiko Akiyama[1], Paul A. Bingham[3], Yingtang Zhou[4, *], Shiro Kubuki[1]

[1]Department of Chemistry, Tokyo Metropolitan University, Tokyo 192-0397, Japan

[2]Mössbauer Effect Data Center, Dalian Institute of Chemical Physics, Chinese Academy of Sciences, Dalian 116023, China

[3]College of Business, Technology and Engineering, Sheffield Hallam University, Howard Street, Sheffield S1 1WB, UK

[4]Institute of Innovation & Application, Zhejiang Ocean University, Zhoushan 316022, Zhejiang, China

*Corresponding authors: Bofan Zhang and Yingtang Zhou

E-mail: 15054218031@163.com (B.F. Zhang); 376477613@qq.com (Y.T. Zhou)

Abstract

Heterojunction catalysts have drawn mounting interest for the visible light-driven Fenton reaction, and bring tremendous opportunities for environmental remediation. Herein, a BiOI/MIL-53(Fe) Z-scheme heterojunction (named BMFe) was synthesized for the first time via a facile strategy. Compared with pristine BiOI and MIL-53(Fe) catalysts, the 2D/3D heterojunction catalyst manifested remarkable catalytic performance toward degradation of phenol, bisphenol A, methylene blue and carbamazepine, which is attributed mainly to the interfacial integration and efficient charge separation. By virtue of coupling at the interface, as confirmed by XPS, ^{57}Fe Mössbauer spectroscopy and DFT calculations, the BMFe catalyst promoted the transfer of electron-hole pairs via Z-scheme and improved the chemical activation of hydrogen peroxide. The subsequent holes, free radicals and nonradical can effectively and continuously decompose pollutants, achieving a positive synergistic effect between photocatalysis and Fenton reactions. Simultaneously, the specially designed BiOX(X=Br, Cl)/MIL-53(Fe) and BiOI/Fe-MOFs(MIL-101, MIL-88) heterojunctions also exhibited advanced oxidative capacity for organic pollutants. Given their practical value for industrial applications, BMFe-beads (1.0 ± 0.15 mm) synthesized via a blend crosslinking method can significantly advance long-term stability and recyclability. The integration of Fe-based metal organic frameworks with bismuth oxyhalide semiconductors provides a new perspective on developing heterojunction catalyst for environmental remediation.

Keywords: Z-scheme; Photo-Fenton reaction; Charge transfer; ^{57}Fe Mössbauer spectroscopy; Beads

Introduction

The Fenton reaction as an efficient advanced oxidation process (AOP) has been widely used in environmental purification applications.[1, 2] However, traditional homogenous Fenton systems are still limited for wider applications by mass iron sludge, narrow pH range and low efficiency of H_2O_2 utilization.[3] Comparatively, the heterogenous photo-Fenton system is receiving a great deal of attention to overcome these drawbacks, which can offer a promising approach with less iron sludge at a wide pH value and efficient Fe^{II}/Fe^{III} cycling.[4] Nevertheless, the efficiency of existing photo-Fenton catalyst is still unsatisfactory for further practical application as it provides less surface reactive sites and unfavorable cycle stability. The design of robust and optimal heterogeneous catalysts with high visible light response, sustainable recyclability and effective charge separation is highly desirable but represents a significant research challenge.

Over the past decade, metal-organic frameworks (MOFs), three-dimensional porous crystals assembled from inorganic metal nodes and rigid multitopic organic links, have brought novelty to the field of porous materials toward wide applications.[5, 6] In particular, the MIL family of MOFs (MIL stands for Material Institute) are built up from chains of M^{III} octahedra connected via organic linkages, forming three-dimensional ordered systems with one-dimensional channel structures along the c-axis.[7] Porous iron terephthalates, denoted $Fe^{III}(OH)\cdot[O_2C\text{-}C_6H_4\text{-}CO_2]$ or MIL-53(Fe) show great potential as heterogeneous photo or photo-Fenton catalysts owing to their highly-ordered structure, non-toxic properties, and broad visible light absorption.[2] Although MIL-53(Fe) is a promising material, its catalytic activity still suffers from drawbacks due to the swift recombination of charge carriers and low efficiency of Fe^{III}/Fe^{II} conversion. To tackle these issues and further improve the catalytic activity of MIL-53(Fe), integration with semiconductors to construct heterojunctions, doping with metal atoms and changing the mole ratio of Fe^{II}/Fe^{III} have

all been considered in previous studies.[8, 9] Among these, Z-scheme heterojunction exhibits high redox potential and effectively suppresses the internal integration of carriers. Specifically, the Z-scheme heterojunction benefited from the two single catalysts with reversible acceptor-donor pair not only significantly inhibit the recombination of photoexcited holes and electrons, but also display outstanding oxidation ability of holes and superior reduction ability of electrons to generate more effective radicals for organic pollutants decomposition.[10, 11] Therefore, the design and synthesis of the MIL-53(Fe) based Z-scheme heterojunctions with semiconductors is a promising choice to realize improved performance.

Bismuth oxyhalide semiconductors, including BiOI, BiOBr and BiOCl, composing of $[Bi_2O_2]$ layers and interleaved by double halogen slabs, been commonly used as photocatalysts.[12, 13] Previous studies have shown that p orbitals are able to access to electronic hybridization in valence band (VB) maximum and conduction band (CB) minimum by theoretical calculations, and that they can thereby promote photocatalytic activity. Among Bi-based semiconductors, BiOI nanosheets with a narrow bandgap of around 1.8 eV display remarkable visible light response.[14] Moreover, the highly anisotropic and favorable crystal structure result in efficient photogenerated h^+ - e^- separation and high mobility of charge carriers. Despite these unique features, BiOI still suffers from limited catalytic activity due to unsuitable energetic edge in the valence band (VB) maximum, which cannot efficiently oxidize contamination by photoinduced holes.[15, 16] Therefore, to improve the oxidative activity by modifying the band structure is an urgent and essential requirement. Interestingly, according to the previous research, it can be seen that the energy band position of BiOI can match well with MIL-53(Fe) and form a staggered structure to achieve advantages of Z-scheme heterojunction. Moreover, the flower-like hierarchical structures of BiOI is more easily to combine and grow 3D bipyramidal material on its sheets and form stable contact

interface between two components. Furthermore, the Fe^{II}/Fe^{III} conversion can maintain at a stable cycle under visible light illumination. Herein, a possible modulation of band structure by fabricating a novel BMFe heterojunction could prove beneficial for utilizing more active centers and efficiently separating charge carries.

Inspired by the above analysis, a novel Z-scheme heterojunction catalyst was synthesized with 3D MIL-53(Fe) bipyramids surrounded by 2D multi-layered BiOI nanosheets via facile procedures, as shown in scheme 1. The BMFe-4 sample showed the highest catalytic activity for the removal of phenol, methylene blue (MB), bisphenol (BPA) and carbamazepine in the presence of H_2O_2 under simulated light illumination. The main oxidative intermediate species, including $\cdot$OH, $\cdot O_2^-/HO_2\cdot$ radicals and $^1O_2$ nonradical were generated over BMFe catalysts and detected by EPR during the photo-Fenton process. Combining XPS and ^{57}Fe Mössbauer spectroscopy, the remarkable charge separation and migration derived from the strong chemical interfacial coupling and the new atomic bonding channel have been elucidated. The efficient mobility of electrons accelerates the conversion of Fe^{III} to Fe^{II} around the catalysts surface, which greatly improves the rate-limiting step in the Fenton reaction. Furthermore, the constructed BMFe-beads possess high stability and recyclability, and used catalysts can be directly separated and then applied to the next cyclic experiment. The regenerable BMFe catalysts bring new potential applications and improved practical value for future industrial and environmental applications of AOP technology.
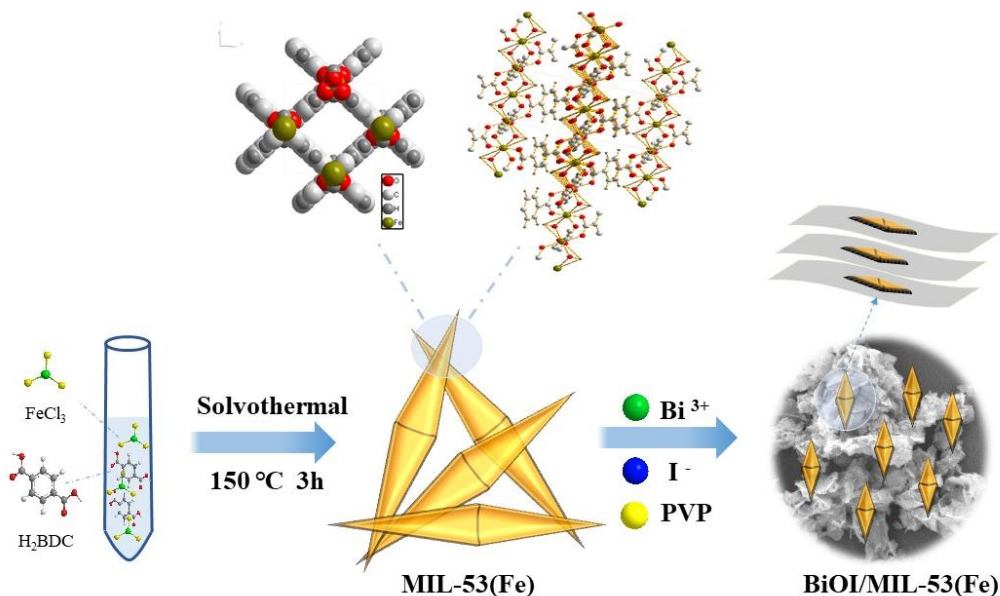
Scheme 1. Schematic diagram of BMFe catalyst synthetic process

2. Experimental section

The details of chemicals, preparation and characterization can be found in the Supporting Information.

2.1 Synthesis of regenerable BMFe beads

Regenerable BMFe-chitosan beads were fabricated via a blend crosslinking process. Specifically, the chitosan was dissolved in 2% (v/v) of acetic acid and stirred until completed dissolved. Then, the prepared BMFe-4 sample was added into colloidal solution and then sonicated for 30 min. The resulting homogeneous solution was injected into 1% NaOH. Then, the guttulate beads were added into NaOH bath for several hours and washed by distilled water until the filtrate was neutral. After that, the BMFe beads within a certain size range (1.0 ± 0.2 mm) were obtained by drying at room temperature for 6 h and are abbreviated as BM-CS.

2.2 Photocatalytic and photo-Fenton activity evaluation

Photocatalytic and photo-Fenton catalytic activity analyses were performed via the degradation experiment using phenol, methylene blue, bisphenol and carbamazepine with a 100

W Hg lamp (λ ≥420 nm) under visible light irradiation. Specifically, H_2O_2 were added into the pollutants solution after reaching equilibrium of absorption and desorption. At certain time intervals, 3 mL of the suspension was measured to establish the concentrations of residual pollutants (The analytic methods are shown in Table S2).

2.3 Apparent activation energy

Apparent activation energy of the BMFe photo-Fenton system was explored at different temperatures (278, 298, 308 and 328 K). The apparent rate constant (k) was obtained at each temperature and the Arrhenius plot was calculated using (1):

$$E_a = RT^2 \frac{dlnk}{dT} = -R\frac{dlnk}{d(1/T)} \tag{1}$$

2.4 Computational parameters

The computational simulations were performed with the plane-wave pseudopotential method based on DFT to probe carrier transfer.[17] The CASTEP code and GGA were applied to explore the interaction and correlation between electron and ion. The optimized parameters of BiOI were a = b = 4.028305 Å and c = 9.759282 Å, and for MIL-53 (Fe) they were observed to be a = 6.9177, b =17.668 Å and c = 12.12 Å. For the interfacial mode of BMFe, a 2×4 surface atomic layers of BiOI (110) was chosen to fit a 1×1 MIL-53(Fe) (111) surface slab. Work functions of BiOI (110) and MIL-53(Fe) (111) surfaces were applied by calibrating the Fermi level to investigate the charge transfer at the interface of BMFe heterojunction.

3. Results and discussion

3.1 Morphology and structure of catalysts

The microstructure of BiOI, MIL-53(Fe) and BMFe were investigated by TEM and SEM measurements. As shown in Figure 1a and Figure S1a, the flower-like structure of BiOI was comprised of numerous layered BiOI nanosheets. The lattice distances of 0.282 nm corresponded

to the highly reactive crystal (110) facets[16] of single-crystal BiOI (Figure 1d). As depicted in Figure 1b and Figure S1b, MIL-53(Fe) is constructed of iron ions and terephthalate anions and displayed uniform bipyramidal structure with a length of 0.2-0.6 μm. The lattice fringe with the spacing of 0.32 nm was matched well with the (111) facet (Figure 1e).[18] The high-magnification TEM and SEM images of BMFe revealed numerous 3D bipyramids closely surrounded by layered 2D nanosheet (Figure 1c and Figure S1c), quite different from pristine BiOI and MIL-53(Fe), which could efficiently prohibit the agglomeration and exposure of more active sites. The calculated lattice spacing of BiOI and MIL-53(Fe) can match perfectly to the individual component and the morphologies were well retained after integration (Figure 1f). Furthermore, energy-dispersive X-ray spectroscopy (STEM-XEDS) was applied to analyze the spatial distribution of BMFe. The spatial position and brightness of Fe, Bi, O and I atoms (Figure S1d) indicated the successful formation of heterostructure composites. The closely-bonded structure can significantly promote charge transfer at the intrinsic interface by reducing charge carries diffusion lengths and inhibit the photogenerated carrier recombination.[19]
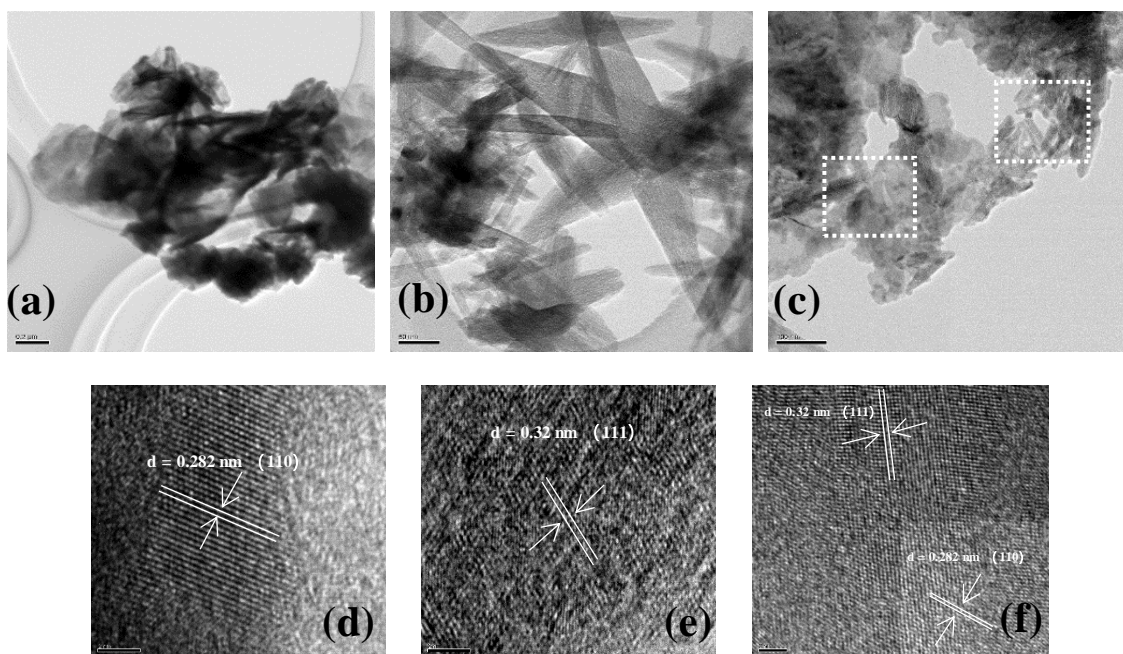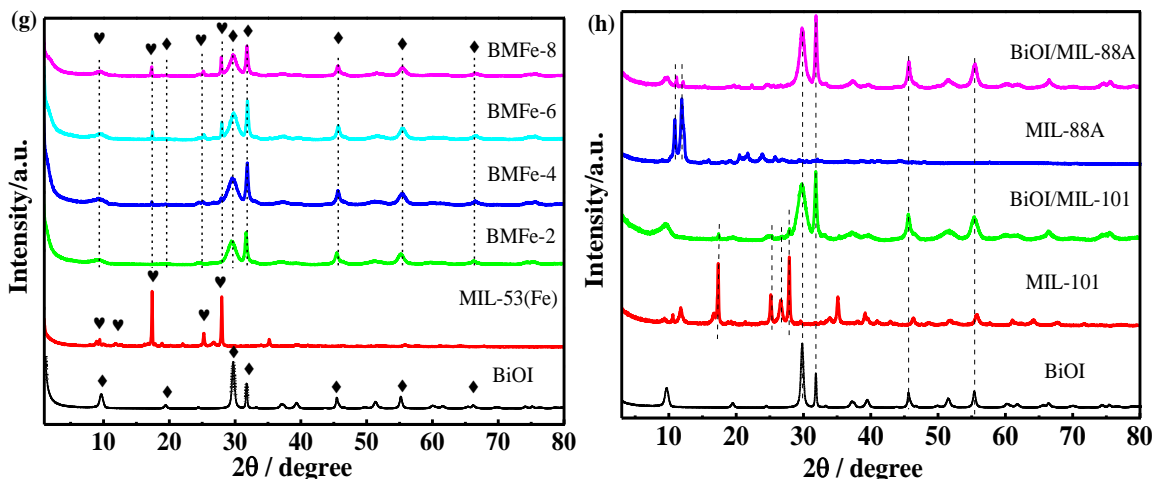
Figure 1. TEM images of (a)(d) BiOI; (b)(e) MIL-53(Fe) and (c)(f) BMFe-4; The scale bar were 200 nm (a), 50 nm (b), 100 nm (c) and 2 nm (d-f), and XRD patterns of prepared catalysts (g-h)

The crystallographic structures of BiOI, MIL-53(Fe) and BMFe were characterized by X-ray diffraction XRD (Figure 1g). For pristine BiOI, the characteristic diffraction peaks located at 2θ=9.65, 19.35, 29.59, 31.74, 45.51, 55.13 and 66.2° were indexed to (001), (002), (102), (110), (200), (212) and (220) planes of BiOI (JCPDS.10-0445), respectively. For BMFe composites, several new diffraction peaks at 9.3, 17.5, 25.3 and 27.7° were detected, ascribed to the crystal phase of MIL-53(Fe), which implies the successful integration of the two components. In addition, with increased loading content of MIL-53(Fe), the intensity of new diffraction peaks gradually increased and the diffraction peaks became broader due to the formation of solid composites with nanocrystalline nature.[20] Furthermore, the PXRD diffraction of BiOI/MIL-88, MIL-101 matched well with the corresponding materials (Figure 1h), indicating the successful synthesis of BiOI/Fe-MOFs composites. In addition, FTIR spectroscopy and thermogravimetric analysis (TGA) were also performed to understand the chemical structure and thermal stability, which further revealed the successful formation of BMFe composites. (Supporting Information, Figure S1e-f, S2a).

3.2 Catalytic activity

The photo and photo-Fenton catalytic activity were firstly evaluated by decomposing cationic

dye under visible light irradiation with/without H_2O_2. As presented in Figure 2a, about 37.7% of MB was degraded by BMFe in 15 min under visible light without H_2O_2. After addition of a certain amount H_2O_2, the degradation rate was dramatically increased to 99%, indicating that H_2O_2 plays a crucial role in removing MB pollutants. In comparison with the high degradation efficiencies of BMFe composites in photo-Fenton system, only 47.1% and 52.2% of MB were removed by pristine BiOI and MIL-53(Fe) in 10 min, suggesting the strong coupling between BiOI and MIL-53(Fe) is a decisive factor. Obviously, the catalytic tendency of BMFe hybrids change over the loading content of MIL-53(Fe) as a volcano curve, and the optimal catalytic performance was obtained by BMFe-4. Furthermore, the highest apparent constant value (*k*) of pseudo-first-order kinetics was calculated to be 0.292 min^{-1} by the BMFe-4 catalyst, which was approximately 2.16, 1.48 and 1.75 times than that of BMFe-2, BMFe-6 and BMFe-8 (Figure S3d). The activity of BMFe heterojunction can be well comparable to the others (Table S3). Notably, the appropriate doping amount of MIL-53(Fe) could offer numbers of iron sites and intrinsic interfacial sites for separation of charge carriers and Fenton oxidation. However, excessive loading amount of Fe-MOFs may result in agglomeration of particles and provoke shielding effects on the surface,[21] eventually weakening the photo-Fenton efficiency.
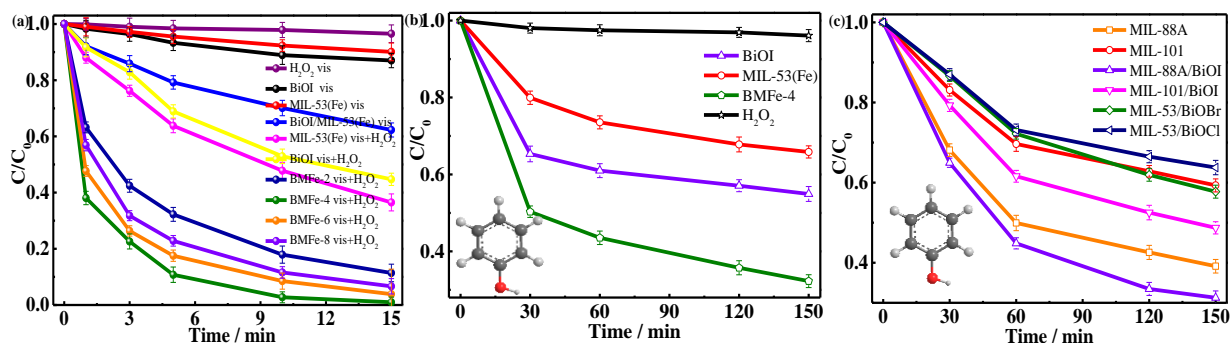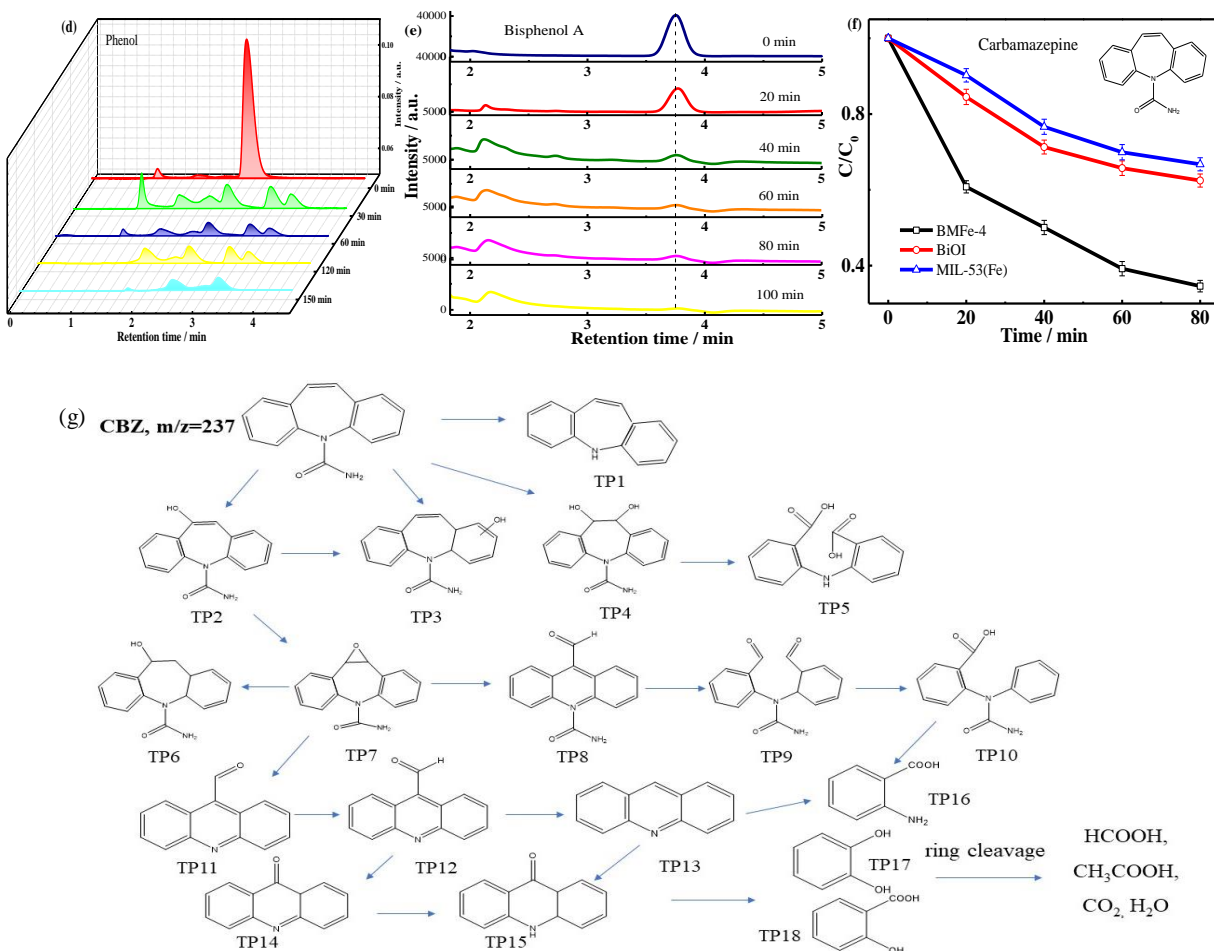
Figure 2. (a)The degradation of MB in the different systems; (b-f) HPLC chromatograms and UV-vis of phenol, bisphenol A, carbamazepine degradation; (g) proposed degradation pathway of carbamazepine (CBZ) by BMFe via H_2O_2 activation under visible light irradiation

It appears that the greatest excellent oxidative property in the photo-Fenton system for MB decomposition was obtained by the BMFe-4 catalyst. To further achieve the optimal reaction conditions, the effects of H_2O_2, pH value, MB concentration and BMFe-4 dosages were investigated, as shown in Figure S3a-c. Since pH is considered the most sensitive factor in Fenton reaction, the effect of initial pH value was explored. As depicted in Figure S3a, MB can be totally removed within 15 min at a wide initial pH range of 3.5-9.5. Under the unadjusted initial pH 5.5 (natural value of BMFe-4 in solution), the catalytic efficiency could maintain a comparable level

11

to that of lower pH 3.5. A slight decrease was found as initial pH increased from 7.5 to 9.5, which was responsible for the occurrence of iron co-precipitation and the weakened activation of H_2O_2. Based on the $Fe^{II}+H_2O_2 \rightarrow Fe^{III}+OH^-+\cdot OH$ process, once iron ion activates H_2O_2, OH^- can be generated. Considering that neutralization of OH^- could cause the reaction proceed in the positive direction under acidic condition,[22] the iron ion cannot be easily complexed with OH^-, resulting in an enhancement in activation of H_2O_2 and MB degradation efficiency. Therefore, the highest removal efficiency and lowest chemical consumption were obtained at pH 5.5, suggesting that no further pH adjustment is required.

The effect of H_2O_2 concentration (0.5-20 mM) is illustrated in Figure S3b. The catalytic efficiency can achieve 99.03% in 15 min under the concentration of 5 mM, which only displayed a slight dip compared to 10 mM (99.21%). As expected, photo-Fenton activity showed a significant decrease with the H_2O_2 concentration increased to 20 mM, which is attributed to the consumption of reactive oxygen species by excess H_2O_2 ($\cdot OH+H_2O_2 \rightarrow \cdot HO_2+H_2O$, $\cdot OH+\cdot HO_2 \rightarrow O_2+H_2O$),[23] resulting in low degradation efficiency and massive consumption of H_2O_2. Therefore, the H_2O_2 concentration of 5 mM was chosen for the following photo-Fenton reaction. Afterward, the impact of BMFe-4 catalyst dosage was investigated, as shown in Figure S3c. With the increase of catalyst dosage, more active sites can participate in the reaction and accelerate the catalytic kinetics. Nevertheless, it can be observed that no significant improvement appeared between 0.5 $g \cdot L^{-1}$ and 0.75 $g \cdot L^{-1}$. Considering the possibility of reduced light transmittance and light scattering by excessive catalyst content,[24] the optimal catalyst concentration was fixed at 0.5 $g \cdot L^{-1}$. Moreover, the reaction kinetics under different conditions were also calculated using the first-order kinetic model and the results are shown in Figure S3e-g. Specifically, the reaction rate constant k with the condition of 5 mM H_2O_2 (0.292 min^{-1}) was 10.1 times faster than that without H_2O_2 (0.029 min^{-1}),

and no obvious difference was found between 5 mM and 10 mM H_2O_2. Meanwhile, the addition of 5 mg BMFe-4 catalyst made the k value 2.28 times greater than with 0.1g/L catalyst and slightly lower than with 1g/L. Therefore, initial pH value and BMFe-4 dosage have obvious influence on the photo-Fenton reaction rate, and the concentration of H_2O_2 significantly determines the number of radical species generated in the BMFe/H_2O_2/hv system. In summary, the optimal conditions for the degradation of MB in the subsequent investigation were as follows: a solution with an initial pH value of 5.5 containing 20 mM MB and 5mM H_2O_2, we add moderate dosages of BMFe-4 to reach 0.5 $g \cdot L^{-1}$ and then irradiated the solution for 15 min under visible light.

To further demonstrate the catalytic potential of as-synthesized BiOX/Fe-MOFs catalysts, refractory pollutants phenol, bisphenol and carbamazepine were supplementary, which could avoid the interference of catalyst sensitized by the dyes. As shown in Figure 2b, the pollutant was hardly degraded in the phenol/H_2O_2/hv system, due to H_2O_2 direct photolysis rate constant is only $1.4 \times 10^{-11} M^{-1}s^{-1}$,[25] reflecting that H_2O_2 cannot be triggered by the only hv to generate ·OH. Compared with pure BiOI (44.03%) and MIL-53(Fe) (34.16%), the removal rate of phenol could achieve to 68.91% by BMFe-4 and the apparent reaction rate constant (k) (Figure S3h-i) was approximately 2 and 3 times than that pristine BiOI and MIL-53(Fe), further confirming the remarkable interfacial coupling between two components. In addition, the catalytic efficiency of two different Fe-based MOFs (MIL-88A, MIL-101) and their composites with BiOI were also evaluated under the same condition. It obviously indicated that MOFs with iron metal nodes and different ligands have different catalytic properties.[26, 27] The Fe-MOFs/BiOI hybrids showed higher efficiency than those pristine Fe-MOFs catalysts. In the MIL-88A system, about 61.9 and 69.8% of phenol were degraded by MIL-88A and BiOI/MIL-88A after 150 min, respectively. The apparent reaction rate constants (k) of BiOI/MIL-88A was 2.6 and 1.3 times larger than BiOI and MIL-88A, respectively.

Similarly, the BiOI/MIL-101 exhibited superior removal rates compared to its individual components, and was 1.4 times greater than that of MIL-101. This result clearly indicates that integration of Fe-MOFs with BiOI semiconductors can achieve strong synergistic effects on the photo-Fenton catalytic process. A similar phenomenon was found in the catalytically decomposed phenol by BiOBr/MIL-53(Fe) and BiOCl/MIL-53(Fe). All BiOX (X=Br, Cl)/MIL-53(Fe) catalysts displayed higher catalytic performance than pure components, indicating the combination of bismuth oxyhalide semiconductor and Fe-MOFs have a positive influence on eliminating organic pollutants. On the basis of above discussion, it can be concluded that semiconductor BiOX/ Fe-MOFs composites can achieve a synergistic intrinsic interaction and remarkably promote the photo-Fenton performance.

The degradation performances of phenol, bisphenol A (a phenolic substance in the plastics industry) and carbamazepine (a tricyclic substance as psychiatric drug) were also investigated via H_2O_2 activation under visible light irradiation. As shown in Figure 2d, the retention time (RT) of phenol was about 2.55 min and the characteristic peak gradually decreased with extension of reaction time. In comparison with phenol solution before reaction, several new peaks gradually appeared at RT 1.72, 1.82, 2.18 and 2.25 min (Figure S4), indicating that phenol was decomposed over BMFe and new intermediates were generated. Similarly, the retention time of bisphenol A was about 3.75 min and the peak intensity decreased obviously after 40 min irradiation and eventually disappeared (Figure 2e). Moreover, some intermediates peaks appeared with the time going (Figure S5), which indicated that the bisphenol A was gradually decomposed under the attack of generated radicals.[28] Meanwhile, the removal rate of carbamazepine over BMFe-4 catalyst reached approximately 67% after 80 min (Figure 2f). The degradation efficiency as significantly enhanced compared with pure BiOI and MIL-53(Fe). Additionally, Figure S6

displayed the mineralization ability of BMFe-4 under removing of MB, carbamazepine, phenol and bisphenol A. The total organic carbon (TOC) removal rates could reach up to 53.2, 46.9, 49.8 and 50.2%, respectively, after 150 min, which exhibiting the superior mineralization and oxidation for aromatic organic compounds. In order to explore the degradation process, high-performance liquid chromatography-mass spectrometry (LC-MS) was used to detect degradation intermediates of carbamazepine in treated solutions (Table S3) and the proposed reaction pathway of CBZ were illustrated in Figure 2g. Specifically, for the carbon and nitrogen attack, the carbamazepine can be directly attacked and formed TP1 and TP2.[5] The generated radical species (h^+, $\bullet OH$, $HO_2 \bullet$, $^1O_2$) during photo-Fenton reaction could attack the olefinic double bond and convert CBZ to TP3 and TP4. Furthermore, most intermediates were continually attacked via ring-opening, N-C bond cleavage and recombination processes to produce TP6-15.[29, 30] Followed by deep oxidation (ring cleavage reaction), small molecular compounds such as TP16-18 were formed and further oxidation result in generation of small carboxylic acid and mineralization products.[31]

To further systematically explore the intrinsic mechanism on the removal of organic pollutants under a visible light-driven Fenton reaction, BMFe was chosen as a model catalyst in the following experiments. Figure S7a presents the physical absorption and chemical degradation by BMFe compared with BiOI and MIL-53 (Fe), as well as material obtained through physically mixed two single powders (B+MFe). During the process of degradation of pollutants, the catalyst is uniformly distributed in the MB solution for physical adsorption determined by their superficial properties. Compared to MIL-53(Fe), the curves of B+MFe and BiOI exhibited a large drop in the adsorption process, and then dropped slowly after adding H_2O_2 (Figure S7a). The corresponding Brunauer-Emmett-Teller (BET) surface area of BiOI, MIL-53(Fe) and BMFe-4 were measured as 10.5, 27.7 and 25.8 m^2/g, respectively (Figure S7c and Table S1). Although the BET surface area

of BiOI is the lowest, it is the most efficient for MB adsorption. The excellent adsorption capacity of BiOI is attributed to the negatively-charged property and two-dimensional layered structure, which can powerfully attract the cationic groups of pollutants.[32] Notably, the BMFe indicates a relatively low adsorption ability but superior degradation ability after the addition of H_2O_2, which was almost completed in 15 min. Comparing the catalytic activity between chemically bonded BMFe and physically mixed B+MFe, the physically mixed composites show better adsorption capacity but lower degradation efficiency, which is mainly derived from the properties of the single components, revealing that no intrinsic coupling existed in physically mixed material. Moreover, the synergetic effect of BMFe was quantitatively evaluated to be 2.56 by synergetic index $C_1 = k_{BMFe}/k_{BiOI} + k_{MIL-53}$, where k is the apparent rate constant under different systems, further confirming the existence of internal interaction in the BMFe catalyst.

Considering that the interfacial interactions could accelerate charge carrier separation and migration, PL spectroscopy and electrochemical impedance spectroscopy (EIS) were performed. As shown in Figure S8a-b, EIS Nyquist plots and PL intensity display regular variation after the combination two monomer catalyst. As expected, the lowest fluorescence intensity and smallest radius of the arc Nyquist plots in EIS occur for the BMFe-4 composite, confirming that it possesses the minimum interfacial impedance on a macrolevel and the fastest charge transfer from the BMFe electrode to the solid/liquid interface to participate in surface reactions.[33] The suppressed photoinduced electron/hole pair recombination and superior charge transfer at the interface are favorable for Fe^{III}/Fe^{II} conversion resulting in efficient photo-Fenton catalytic performance.

To identify the synergistic effect of heterojunction BMFe in the process of photo-Fenton catalytic degradation of MB, thermodynamic apparent activation energy (E_a) of different systems (BiOI, MIL-53, BMFe) were calculated. As depicted in Figure S9, the E_a of BMFe was calculated

to be 7.91 J/mol by the linearly correlated Arrhenius plot, which decreased more than 49.4% and 71.5% relative to that of pure BiOI (15.64 J/mol) and MIL-53(Fe) (27.77 J/mol). Generally, surface reactions with a longer time-scale (ms ~ s) are the rate-determining steps during the photo-Fenton process. The decreased activation energy and the faster carrier transfer indicate that surface reaction has converted from the single catalyst surface to the interface between BiOI and MIL-53(Fe), thereby the rate-determining step was efficiently accelerated.[34] Taking into account the chemical coupling, BMFe heterojunction could reduce the reactive barrier and facilitate the reaction to diffusion control.

3.3 Catalytic mechanism

The surface state and local structure of Fe active sites are essential to the Fenton catalytic activity. To investigate the coordination environment of iron species before and after integration of BiOI, high-resolution XPS and ^{57}Fe Mössbauer spectroscopy were carried out. As shown in Figure 3a-b, the characteristic XPS peaks at 711.4 eV and 725.1 eV, as well as the satellite signal at 719.2 eV belong to Fe $2p_{3/2}$ and Fe $2p_{1/2}$ of Fe^{III}. For BMFe-4, a satellite peak located at 728.8 eV appeared and all the peaks corresponding to 710.72, 724.43 and 717.11 eV shifted to lower binding energies compared with pristine MIL-53(Fe) crystal. This behavior was attributed to chemical interactions between the iron oxide and BiOI nanosheets. Previous studies reported that the strong interaction between two crystals could facilitate electron transfer via an atomic interface-bonding channel, which would generate defect energy levels, and eventually increase the charge density.[35, 36] Therefore, the negative binding energy shifts and extra satellite peak in the Fe 2p spectrum of BMFe-4 are related to the increased outer electron cloud density and the formation of new bonds at the interface, which can significantly modify the band structure of composites and favor charge transfer during the catalytic reaction.

Considering that [57]Fe Mössbauer spectroscopy is a sensitive and powerful technique for detecting the variation in oxidation state and coordination environment of iron atoms,[37] which can further confirm the structural changes after integration of BiOI. As shown in Figure 3c-d, the quadrupolar hyperfine structures can be fitted as a superposition of one symmetric doublet and slightly different values for δ and Δ were obtained after combination with BiOI. The isomer shift is associated with the oxidation state of iron ion, while quadrupole splitting is a measure of *s*-electron density around the Fe nucleus and consequently illustrates the symmetry of the space charge distribution near the Fe nucleus.[38] The isomer shift values obtained from the corresponding hyperfine parameters (Table.1) indicate that the a high-spin of octahedral ferric irons (FeO_6) exist in the metal-organic framework. It is known that corner-sharing *trans*-chains of octahedra iron connected with terephthalic acid construct an open metal-organic framework and the bond length of the octahedral $Fe-O_{av}$ are approximately 2.0 Å.[39] The variations of isomer shift and quadrupolar splitting suggest that the local electron density and coordination environment of Fe were subject to subtle alterations in bond angles or distances after formation of BMFe. During the synthesis of composites, the M-O-M chains (M=Fe) in the MOF material can be disrupted to some extent upon introduction of BiOI and small changes in the bond angles/distances could be attributed to the newly-formed M1-O-M2 chains (M1=Fe, M2=Bi), leading to expansion of the building unit by several Å. Moreover, the dramatically enhanced photo-Fenton behavior depends on the dopant amount of Fe-MOF, suggesting that interfacial properties with appropriate bonding joint is essential to catalytic activity.

(a) Fe 2p$_{3/2}$ 711.44 eV, Fe^{3+} Statellite, Fe 2p$_{1/2}$ 725.14 eV, MIL-53(Fe) Fe 2p

(b) Fe 2p$_{3/2}$ 710.72 eV, Fe^{3+} Statellite, Fe 2p$_{1/2}$ 724.43 eV, BMFe-4 Fe 2p

(c) Signal, Fe^{III}

(d) Signal, Fe^{III}

(e) DMPO-·OH, Light, Dark

(f) DMPO-HO$_2$·/·O$_2^-$, Light, Dark

(g) TEMPO-^{1}O$_2$, Light, Dark
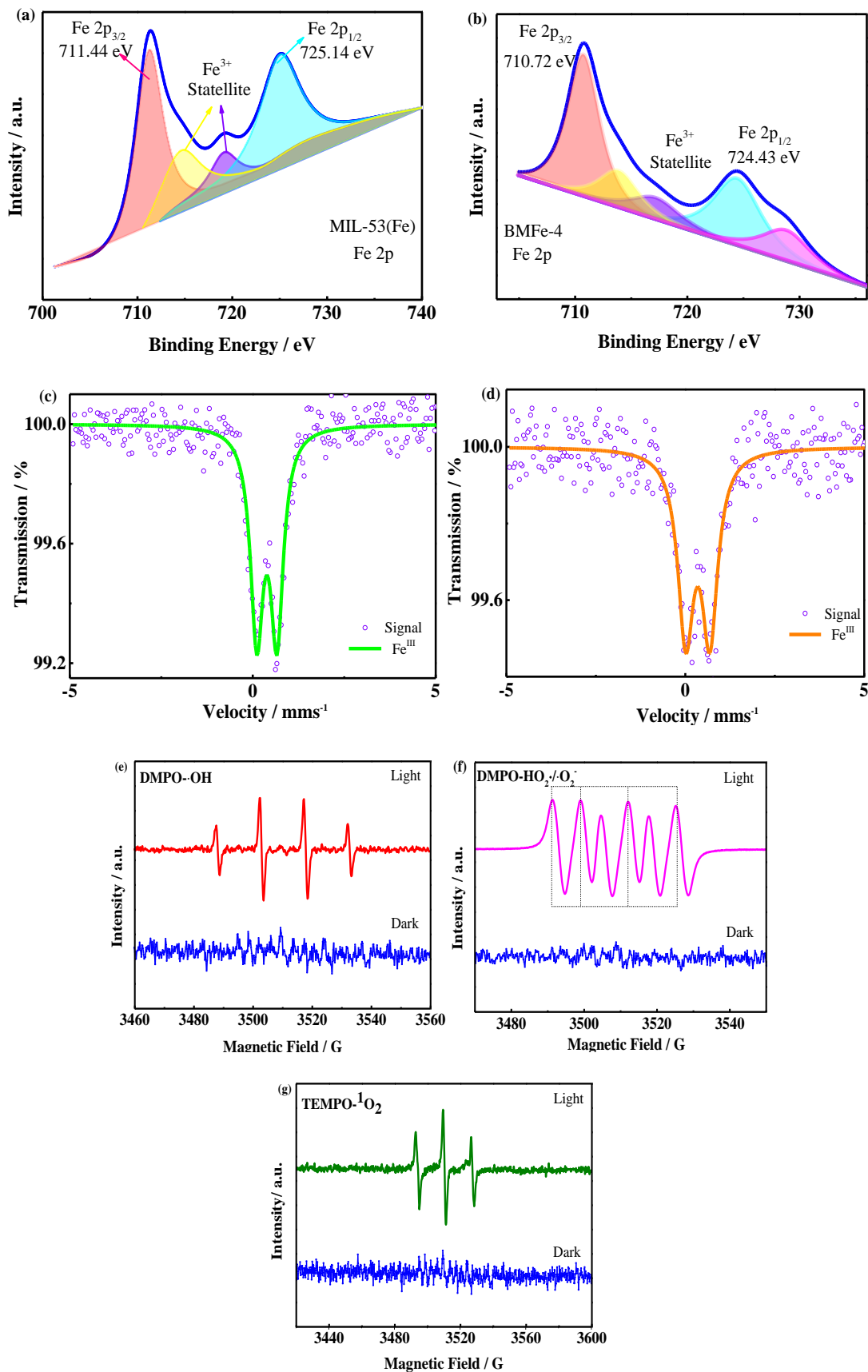
Figure 3. High resolution XPS spectra of Fe 2p for MIL-53(Fe) (a), BMFe-4 (b); Room temperature

Mössbauer spectra for MIL-53(Fe) (c) and BMFe-4 (d); EPR spectra of (e) DMPO- •OH, (f) DMPO- •O_2^-/

HO_2•, (g) TEMPO- $^1O_2$ for BMFe-4 catalyst

Table 1. Room temperature ^{57}Fe Mössbauer hyperfine parameters of MIL-53(Fe) and BMFe

Sample	δ (mm/s)	Δ (mm/s)	Line Width (mm/s)	Spectral Area (%)	Assignment
MIL-53(Fe)	0.386	0.55	0.42	100	Octahedral Fe^{III}
BMFe-4	0.349	0.68	0.53	100	Octahedral Fe^{III}
After reaction BMFe-4	0.369	0.65	0.45	100	Octahedral Fe^{III}

(IS δ: isomer shift; QS Δ: quadrupole splitting; Line width: half peak width; Spectra area: absorption area proportion)

The pathways involved in the photo-Fenton catalytic process contain pollutant absorption, optical excitation, charge transfer and redox reaction. To explore the oxidation mechanism of the BMFe for degradation of pollutants, reactive radical and nonradical species during the photo-Fenton process were considered. It is well known that the Fenton or photo-Fenton reaction is based on the formed OH, •O_2^-/ HO_2•, $^1O_2$ and h$^+$ reacting with the organic contaminants.[40] Theses radicals can be transformed into each other during the reaction. In particular, •OH can convert into $^1O_2$ by the disproportionation reaction (equation 2), •O_2^- can transform into •OH by Haber-Weiss reaction (equation 3).[23] Moreover, there is a conversion between •O_2^- and $^1O_2$ by equation 4.

$$4 \cdot OH \rightarrow {}^1O_2 + 2H_2O \qquad (2)$$

$$\cdot O_2^- + H_2O_2 \rightarrow \cdot OH + OH^- + O_2 \qquad (3)$$

$$\cdot O_2^- + \cdot OH \rightarrow {}^1O_2 + \cdot OH^- \qquad (4)$$

$$\cdot O_2^- + H^+ \rightarrow HO_2 \cdot \qquad (5)$$
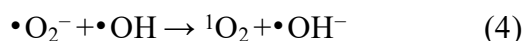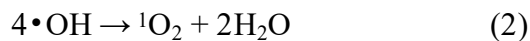
Electron paramagnetic resonance (EPR) is an efficient technique for detecting $\bullet$OH, $\bullet O_2^-$/ $HO_2\bullet$ and $^1O_2$ using 5,5-dimethyl-pyrroline-N-oxide (DMPO)-H_2O solvent, DMPO-CH_3OH solvent and 2,2,6,6-tetramethylpiperidine (TEMP), respectively.[23] As shown in Figure 3e-g, the EPR spectra of BMFe-4 did not exhibit obvious resonance attributable to $\bullet$OH, $\bullet O_2^-$/ $HO_2\bullet$ and $^1O_2$ under dark conditions. After irradiating for 5 minutes, four split lines (symmetry center: g=2.0055, a_N=14.9G, a_H=14.9G, intensity ration 1 : 2 : 2 : 1) for $\bullet$OH radical, hyperfine splitting constants (a_N=14.9G, a^{α}_H=10.38G and a^{β}_H=1.31G) for $\bullet O_2^-$/ $HO_2\bullet$ radical and typical triplet peak signal (g=2.0054, a_N=16.9G,) for $^1O_2$ nonradical were obtained.[23] This result indicates that BMFe-4 catalyst can convert the above three radicals under a visible light-driven Fenton process.

To investigate the catalytic effect by these radicals in the photo-Fenton reaction, isopropyl alcohol (IPA), benzoquinone (BQ), triethanolamine (TEOA) and sodium azide (NaN$_3$) were added to capture the $\bullet$OH, $\bullet O_2^-$/ $HO_2\bullet$, h^+ and $^1O_2$, respectively.[41] As depicted in Figure S10, all of these scavengers had a certain negative effect on the degradation of MB. For instance, with the concentration of TEOA increased, the removal efficiency of MB decreased significantly, implying that h^+ was one of the main active species. The apparent kinetic constants k under six different concentrations of TEOA were calculated by the equation of $\ln(C/C_0)$ =-kt. When the concentration of TEOA increased to 0.8 and 1.6 mM, there was no significant variation of removal rate, indicating the constant k reached its limiting value. Accordingly, the limit of removal efficiency by h^+ was estimated at 38.01% ($\frac{0.292-0.181}{0.292}$). Similarly, the reactive oxygen species of $\bullet$OH, $\bullet O_2^-$/ $HO_2\bullet$, and $^1O_2$ do have a university in BMFe/H_2O_2 photo-Fenton system, for which the limited effects were 32.2%, 25.3% and 15.75%, respectively. Interestingly, the total efficiency of the four active radical species was more than 100%, which was ascribed to the rapid interconversion

between these reactive oxygen species ($\cdot$OH, $\cdot O_2^-/HO_2\cdot$, and $^1O_2$) in the photo-Fenton system. Based on this result, it can be concluded that h^+, $\cdot$OH and $\cdot O_2^-/HO_2\cdot$, play the major roles in the removal of MB and the $^1O_2$ is a supporting active species.

Although considerable reactive oxygen species of $\cdot$OH, $\cdot O_2^-/HO_2\cdot$ and $^1O_2$ are generated in the photo-Fenton system, the detailed transfer pathway of the reactive radicals and heterostructure between the two types of photocatalysts are still unclear in the oxidation process. To clarify this point, the band structure and relative band edge of two single catalyst were measured. As depicted in Figure S11a, UV-vis DRS of the catalysts displayed excellent absorption in the region of 400-600 nm, and the light absorption edge showed a clear red-shift after coupling with BiOI, indicating that the light-harvesting ability correspondingly improved. The bandgap energies (E_g) were evaluated using the Kubelka-Munk method[42] and were measured to be 1.79 and 2.72 eV, respectively. Further, the flat band edge was investigated by M-T and XPS measurements. As shown in Figure S11b-c, the CB and VB are estimated at approximately -0.78 (BiOI) and 2.49 eV (MIL-53(Fe)), respectively. Combined with the bandgap energy (E_g) of BiOI and MIL-53(Fe) from UV-vis absorption data, VB and CB potentials were 1.01 and -0.23 eV. Correspondingly, the energy band structures of BiOI and MIL-53(Fe), as well as other Fe-MOFs and BiOX catalysts are presented in Figure S11d. As depicted in Figure S12a, after addition of IPA, TEOA and BQ, the catalytic performances were inhibited to a certain extent, illustrating that all of these h^+, $\cdot$OH and $\cdot O_2^-(HO_2\cdot)$ radicals existed in removing pollutants under visible light irradiation.

According to the staggered band structure and active radicals scavenging that results in photocatalytic systems without H_2O_2, two possible carrier transfer mechanisms are proposed: Direct Z-scheme and Type-II heterojunction (Figure S12b-c). In traditional Type-II heterojunction, the photoexcited e^- in the CB of BiOI can migrate to the CB of MIL-53(Fe), while photoexcited

h[+] tend to transfer from the VB of Fe-MOF to the VB of BiOI. By this transport mode, the photogenerated e[-] cannot reduce O_2 to $\cdot O_2^-$/ $HO_2\cdot$ due to the CB potential of MIL-53(Fe) (-0.23 eV) being more positive than the standard value of O_2/$\cdot O_2^-$/ $HO_2\cdot$ (-0.33eV). Furthermore, the VB potential of BiOI (1.01 eV) is more negative than the H_2O/$\cdot OH$ (2.38 eV), reflecting that BMFe cannot oxidize H_2O to $\cdot OH$ under photoexcited h[+]. Accordingly, based on the transport mechanism of Type-II heterojunctions, it is unfavorable for the active radical species ($\cdot O_2^-$/ $HO_2\cdot$, $\cdot OH$) detected by the scavenging experiment in the BMFe photocatalytic process without H_2O_2. Contrarily, through the direct Z-scheme charge pathway, the photogenerated e[-] tend to migrate from the CB of Fe-MOF to the VB of BiOI via a solid/solid heterointerface until in equilibrium.[43] The spatially separated e[-] in the CB of BiOI and h[+] in the VB of MIL-53(Fe) can efficiently reduce O_2 to $\cdot O_2^-$/ $HO_2\cdot$ and oxidize H_2O to $\cdot OH$, respectively, which is consistent with the radical scavenging results. The Z-type feature significantly enhances the carrier transfer efficiency and thus improves the removal rate of pollutants by BMFe.

To further investigate the charge carrier pathway, the energy-band structures and charge migration of BMFe heterojunction were calculated based on DFT. Generally, work functions (Φ) of catalysts can be calculated by the followed formula: $(\Phi) = EV_{ac} - E_f$, (EV_{ac} is the energy level of electron, E_f is the Fermi energy level of the semiconductor). The calculated work functions of BiOI (110) and MIL-53 (Fe) (111) are 6.19 and 7.23 eV (vs. Vacuum), respectively (Figure 4a-c). Moreover, the work function can be also extracted from the Ultraviolet photoelectron spectroscopy (UPS) measurement. The value of work function indicates the minimum energy for an electron (e[-]) from the surface to the edge of vacuum. Owing to that the value of work function decided by the structure and chemical composition of catalysts, it is an important piece of property in catalytic

process and catalysts surface analysis. As depicted in Figure 4d-e, the UPS spectra for the secondary electron cut-off values of two pure catalysts were obtained. The corresponding work function value can be calculated based on the following equation:

$$\Phi = h\nu - E_{cutoff} - E_f \qquad (6)$$

where the Φ, $h\nu$, E_{cutoff} and E_f are the value of work function, the photon-energy of helium gas (He 1 UV emission at 21.2 eV), the secondary electron cut-off values and the Fermi edges, respectively. Generally, the E_f was almost near to zero (the inserted figures) and the Φ value can be calculated by the $h\nu$ and E_{cutoff}. Figure 4d-e displayed that the photoemission cutoff of MIL-53(Fe) is 14.06 eV corresponding to a work function of 7.14 eV, while the work function of BiOI is estimated to be 6.01 eV. These values are almost consistent with the Φ values calculated by DFT analysis. As shown in Figure 4c, through the analysis of the edge position, it can be observed that the Fermi level of BiOI is near to the VB, while MIL-53(Fe) is closed to the CB. After integration, MIL-53(Fe) is an electron donor and the BiOI is an electron acceptor.[44] Electronic DOS (Figure S15) and Charge of difference show that pure BiOI and MIL-53(Fe) possess a staggered band structure and the carrier mobility of BMFe heterojunction follows Z-scheme mechanism,[45] which can achieve effectively separation of charge carriers during the photo-Fenton reaction. Additionally, an asymmetric built-in electric filed at the interface of BMFe heterojunction could reduce the work function and is regarded as the main reason for the efficient separation h^+-e^- in the heterojunction.[17] Therefore, based on this simulation analysis of band edge position and charge carrier migration, the flow of electrons from MIL-53(Fe) to BiOI is consistent with Z-scheme pathway.
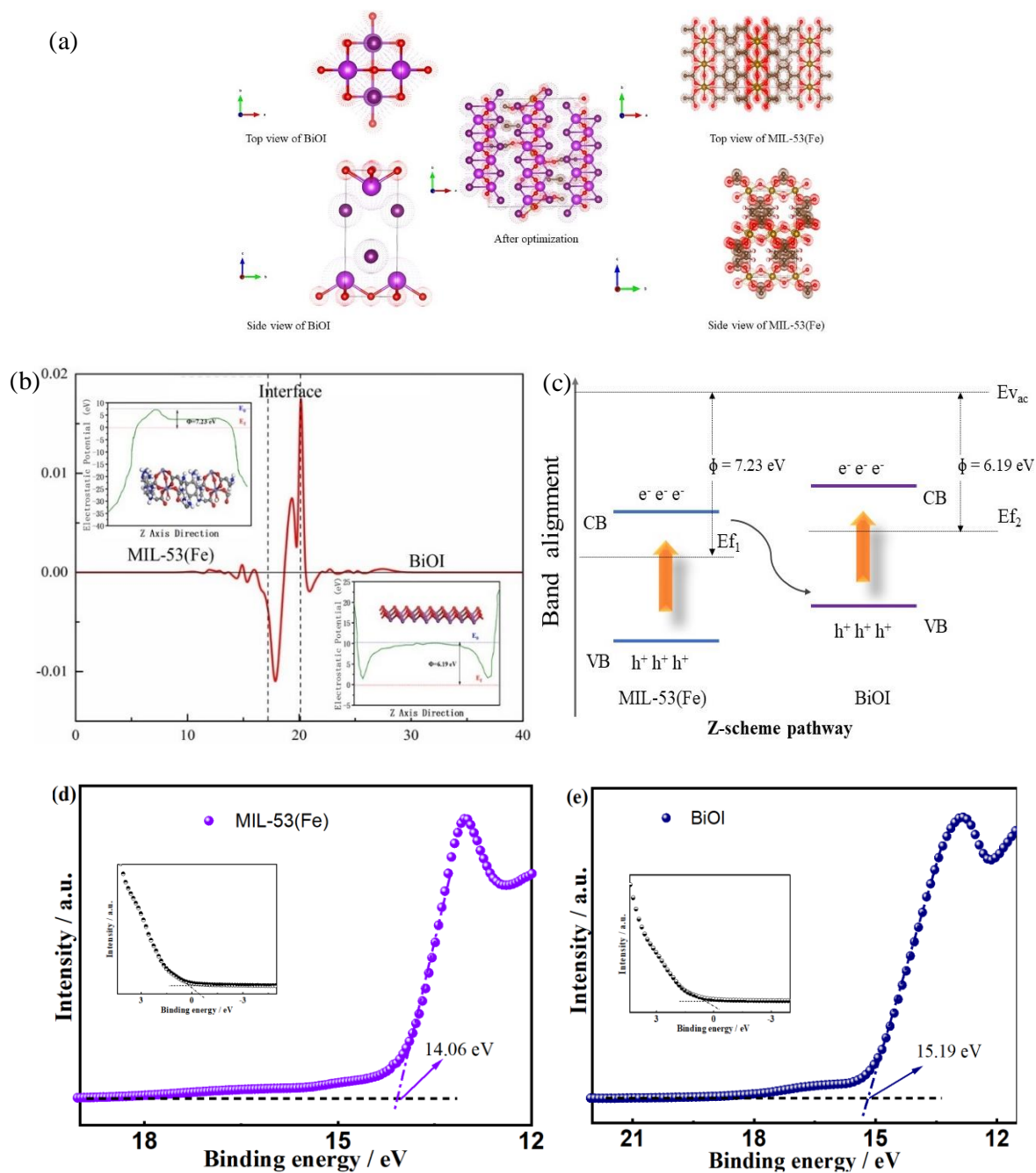
Figure 4. (a) Top view and Side view of BiOI (110) plane (2×4 atomic layers, a = b = 4.028305 Å and

c = 9.759282 Å) and MIL-53(Fe) (111) plane (1×1) atomic layer, a = 6.9177, b = 17.668 Å and c = 12.12 Å); (b)

Work function and electrostatic potential of BiOI, MIL-53(Fe); (c) Band alignment of BMFe based on first-

principle calculations; (d-e) UPS profile, the insets show the fermi edges

Based on the above analysis, during photo-Fenton reaction, benefiting from appropriate

interfacial contact between two single catalysts, BMFe heterojunction exhibited much enhanced charge separation efficiency and thus improved the catalytic performance compared to single catalyst. When visible light irradiated on BMFe composite, the left e^- and h^+ could react with O_2 to produce $\bullet O_2^-/HO_2\bullet$ radicals and then immediately oxidize organic compounds, respectively. Simultaneously, the generated electrons (e^-) and Fe sites can combine with H_2O_2 to form OH, $\bullet O_2^-/HO_2\bullet$ radicals and $^1O_2$ nonradicals. The subsequent holes, free radicals and nonradical can effectively and continuously decompose organic pollutants, achieving a positive synergistic effect between photocatalysis and Fenton reactions. Furthermore, the generated electrons in the conduction band can rapidly transfer and reduce Fe^{III} to more active Fe^{II} on the catalyst surface. Throughout this process, the Z-scheme heterojunction BMFe catalyst greatly improved the rate limiting step in the traditional Fenton reaction and achieves superior catalytic activity. The reaction process of reactive radicals during pollutants purification is summarized and illustrated in the following Equation:

$$BMFe + h\nu \rightarrow e^- + h^+ \qquad (7)$$

$$H_2O_2 + e^- \rightarrow \bullet OH + OH^- \qquad (8)[46]$$

$$e^- + O_2 \rightarrow \bullet O_2^- \qquad (9)[47]$$

$$Fe(III) + H_2O_2 \rightarrow Fe(II) + HO_2\bullet + H^+ \qquad (10)[46]$$

$$Fe(II) + H_2O_2 + H^+ \rightarrow Fe(III) + \bullet OH + H_2O \quad (11)[46]$$

$$Fe(III) + e^- \rightarrow Fe(II) \qquad (12)[48]$$

$$HO_2\bullet + H_2O_2 \rightarrow \bullet OH + H_2O + O_2 \qquad (13)[46]$$

$$4\bullet OH \rightarrow {}^1O_2 + 2H_2O \qquad (14)[47]$$

$$\bullet O_2^- + H_2O_2 \rightarrow \bullet OH + OH^- + O_2 \qquad (15)[23]$$

$$\bullet O_2^- + \bullet OH \rightarrow {}^1O_2 + OH^- \qquad (16)[47]$$

$$\bullet O_2^- + H^+ \rightarrow HO_2 \bullet \qquad\qquad (17)^{47}$$

$$\bullet OH/HO_2 \bullet /^1O_2/h^+ + MB/phenol/bisphenol\ A/carbamazepine \rightarrow small\ molecules\ (18)$$
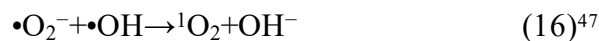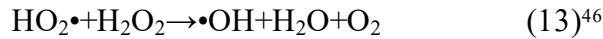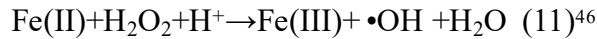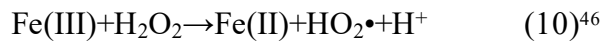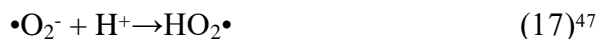
3.4 Photocompensation of Fenton catalyst and stability testing

Generally, three-dimensional porous MIL-53(Fe) with 1D linkages of -Fe-O-Fe- and bis-bidentate terephthalate links could serve as catalysts to active peroxides with or without light illumination. Herein, the catalytic performance of BMFe composite prepared in this work was measured under a dark environment. As depicted in Figure 5a, BMFe-4 can efficiently activate H_2O_2 to degrade MB in the dark, and was almost complete after 50 min, indicating that BMFe-4 can achieve light-independent wastewater treatment. However, after five cycles in the dark, the degradation of MB decreased significantly, which might be attributed to a large amount of active sites of Fe^{III} being covered by organic pollutants in the Fenton system.[49] According to the mechanism of photocatalysis, the generated electrons in the conduction band (CB) can rapidly transfer and reduce Fe^{III} to more active Fe^{II} on the catalyst surface (the potential of Fe^{III}/Fe^{II} is 0.77V),[41] and free radicals generated by photoelectrons and holes could also decompose organic pollutants, including but not limited to contaminants covering the active sites, which eventually reactivate the Fenton reaction. Based on this point, the weakened efficiency was relieved after giving 15 min of visible light illumination, and the degradation rate could be maintained at a stable level of 85.1% after 3 cycles. The d-orbital of reduced Fe^{II} can overlap partially with sp^3-hybrid orbital of O-O, resulting in the electron of Fe^{II} being transferred to H_2O_2 more easily. The elongated and weakened O-O bond of H_2O_2 could efficiently generate more $\bullet OH$ to degrade pollutants.[50] Throughout this process, the Z-scheme heterojunction BMFe catalyst greatly improved the rate limiting step in the traditional Fenton reaction and achieves a stable dark-light cycle.

The stability and recyclability of catalysts are essential factors before applying into practical wastewater treatment, so five-cycle experiments were conducted under visible light for MB degradation. After using for 5 cycles, the catalytic activity of BMFe-4 gradually decreased from 99.6% to 82.7% (Figure S13a). The total leached iron concentration after each cycle ranged from 0.22 to 0.39 mg/L and significantly lower than European wastewater discharge standard (2 mg/L) (Figure S13b). The catalytic effect of leached Fe ions in homogeneous reaction was much lower than that of BMFe heterojunction (Figure S13c), illustrating the negligible effect of leaked iron and the dominant role of the heterogenous reaction. To explore the reduced catalytic performance of BMFe-4, ^{57}Fe-Mössbauer spectroscopy, XRD, BET and FTIR analyses were carried out. Figure S13d shows that the diffraction peak intensities of BMFe-4 only decreased slightly and no new diffraction peaks appeared in the XRD diffraction pattern of the used sample, which indicates that the crystal structure has no significant change following reaction. The surface area of used BMFe-4 was measured as 21.4 m^2/g (Table S1), which is slightly lower than the fresh sample. The decreased surface area may be ascribed to the physical adsorption of dyes into its internal pores. The FTIR spectrum shows that the peak at 3440 cm^{-1} is obviously stronger for the fresh BMFe-4 than for the used BMFe-4 (Figure S13e). Meanwhile, the intensities of the peaks at 1282 and 1673 cm^{-1} became weaker for the used BMFe-4 than for fresh BMFe-4, similar to the pristine BiOI, indicating that the coordinated interaction between BiOI and MIL-53(Fe) slightly weakens after being reused. Further, the ^{57}Fe Mössbauer spectra for the fresh and used catalysts were also recorded at ambient temperature (Figure 5b). The hyperfine parameters obtained from the fitting of Mössbauer spectra as one symmetric doublet are slightly different after 5 cyclic experiments. Such variations in the isomer shift suggests that the bonding interaction or the nature of O atoms as the first neighbors of Fe sites has changed.[51] The slightly decreased value of quadrupole splitting

is more similar to that of pristine MIL-53(Fe), suggesting that the electronic charge distribution near Fe sites was modified. The observation of coordination environment of iron sites indicates that the coupling effect between BiOI and MIL-53(Fe) was weakened, consistent with the above discussion of FTIR results. Nevertheless, the typical high spin Fe^{III} with first neighbors of O atoms in an octahedral structure was still retained after reaction. Considering the rate-limiting step (Fe^{III} + $H_2O_2 \rightarrow Fe^{II}$ + $HO_2 \bullet$ + H^+), the total Fe^{III} signal indicate that the ferrous iron generated during the reaction was completely oxidized into iron oxides or ferric iron after 5 cycles. Although some of the Fe^{III} can be reduced by photogenerated e^- in BMFe Z-scheme heterojunctions, the complete conversion of Fe^{II}/Fe^{III} and mass loss of the catalyst became limiting factors and induced significant decreases of catalytic efficiency under long-time visible light illumination.
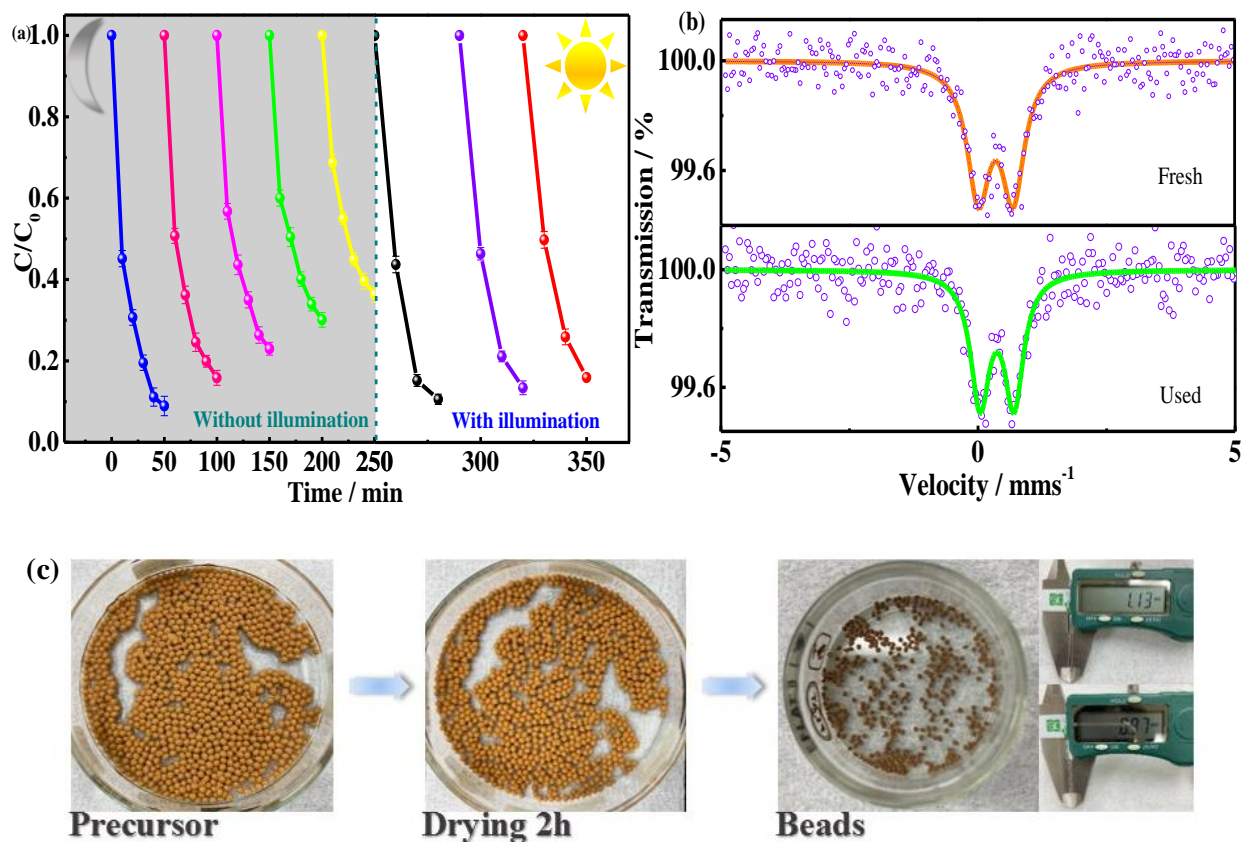
Figure 5. (a) Stability test of BMFe-4 under without illumination and after illumination, (b) Room temperature ^{57}Fe Mössbauer spectra, (c) The synthesis process on the average size of BMFe-beads

On the other hand, the catalytic efficiency of fine or ultrafine powder catalysts usually decreased obviously after several cycles due to mass loss. Although heterogeneous BMFe catalyst can be regarded as a potential material applied in wastewater treatment, the loss of quality and difficulty in regeneration restrict it for practical industrial applications. To achieve a more stable and wider utilization, immobilization of the powder catalyst on a support is an efficient strategy for multiple recycles. Chitosan (CS) has been widely used as support due to its biocompatibility, non-toxicity and biodegradable properties.[52, 53] In addition, it possesses a stable chain-like structure and can be easily used to formulate beads.[54] Herein, BMFe-CS beads were synthesized via a simple blend crossing strategy. As shown in Figure 5c, the undried BMFe-CS precursors were yellow-brown beads with a uniform diameter of 2.0±0.10 mm. After drying, the color of the beads became dark brown and the diameter was reduced to 1.0±0.15 mm. The smaller size can expose more reactive sites to participate in photo-Fenton reaction and the spherical beads can be easily separated by filtration.

To evaluate the catalytic performance and stability of the BMFe-CS beads, methylene blue was used as simulant pollutant, with testing performed in a glass beaker under visible light illumination. Figure S14a reveals the activity and stability of BMFe-CS beads for eight consecutive cycles. No significant decreases in the catalytic performance for MB removal were observed. The degradation rate remains approximately 98% after 8 times of repeated use and the mass changed less than 5%. The reused beads were collected and characterized using XRD. Compared with fresh beads, no change was observed in the XRD diffraction peaks (Figure S14b), indicating that the crystal structure was strongly-retained. The above results suggest that BMFe-CS beads have high stability and reusability which could potentially meet the needs of practical utilization for wastewater treatment.

4. Conclusions

This work reports a facile two-step solvothermal and precipitation strategy to synthesize a novel 2D/3D BiOI NSs/MIL-53(Fe) heterojunction for light-driven Fenton oxidation. Bipyramidal MIL-53(Fe) was steadily combined with hierarchical BiOI NSs to form Z-scheme heterojunctions, exhibiting fast charge carrier separation and transfer across the interfacial bonding channel. Compared with pristine catalyst, the BMFe Z-scheme heterojunction exhibited remarkable catalytic activity for MB, phenol, bisphenol A and carbamazepine degradation in a wide pH range by the subsequently-formed h^+, $\cdot OH$, $HO_2 \cdot$ and $^1O_2$ active species. High continuous charge carrier migration and separation induced efficient conversion of Fe^{III}/Fe^{II} and promoted the synergistic effects between photocatalysis and activation of hydrogen peroxide, which obviously changed the reaction kinetically and thermodynamically. In addition, the regenerable BMFe beads displayed remarkable long-term stability and recyclability, promoting BMFe as a promising catalyst for large variety of industrial applications in the future.

Supporting Information

Chemicals, Synthesis of Fe-MOF and Fe-MOF/BiOX catalysts, Characterizations; BET surface areas and pore diameters, Details of the analysis of pollutants; Degradation intermediates of CBZ; Comparison of catalytic performance with series of previously reported catalysts; SEM images, FT-IR spectra; TGA curves and XPS spectra; Different influencing factors; HPLC chromatograms of phenol and Bisphenol A degradation; Mineralization rate of organic pollutants; N_2 adsorption-desorption curves; EIS Nyquist plot and PL spectra; Apparent activation energy for MB degradation; Effect of reactive species; UV-vis DRS; Band spectra; Stability test of BMFe and BMFe-beads; Band-structure and density of states based on DFT calculation.

Acknowledgements

References

(1)   Ren, Y.; Shi, M.; Zhang, W.; Dionysiou, D. D.; Lu, J.; Shan, C.; Zhang, Y.; Lv, L.; Pan, B., Enhancing the Fenton-like Catalytic Activity of nFe_2O_3 by MIL-53(Cu) Support: A Mechanistic Investigation. *Environ Sci Technol.* **2020,** *54*, 5258-5267.

(2)   Sharma, V. K.; Feng, M., Water Depollution using Metal-Organic Frameworks-Catalyzed Advanced Oxidation Processes: A Review. *J Hazard Mater.* **2019,** *372*, 3-16.

(3)   Sun, H.; Xie, G.; He, D.; Zhang, L., Ascorbic Acid Promoted Magnetite Fenton Degradation of Alachlor: Mechanistic Insights and Kinetic Modeling. *Applied Catalysis B: Environmental.* **2020,** *267*, 118383.

(4)   Ma, C.; Feng, S.; Zhou, J.; Chen, R.; Wei, Y.; Liu, H.; Wang, S., Enhancement of H_2O_2 Decomposition Efficiency by the Co-Catalytic Effect of Iron Phosphide on the Fenton Reaction for the Degradation of Methylene Blue. *Applied Catalysis B: Environmental.* **2019,** *259*, 118015.

(5)   Li, Y.; Yang, Y.; Lei, J.; Liu, W.; Tong, M.; Liang, J., The Degradation Pathways of Carbamazepine in Advanced Oxidation Process: A Mini Review Coupled with DFT Calculation. *Science of The Total Environment.* **2021,** *779*, 146498.

(6)   Cheng, M.; Lai, C.; Liu, Y.; Zeng, G.; Huang, D.; Zhang, C.; Qin, L.; Hu, L.; Zhou, C.; Xiong, W., Metal-Organic Frameworks for Highly Efficient Heterogeneous Fenton-Like Catalysis. *Coordination Chemistry Reviews.* **2018,** *368*, 80-92.

(7)   Bavykina, A.; Kolobov, N.; Khan, I. S.; Bau, J. A.; Ramirez, A.; Gascon, J., Metal-Organic Frameworks in Heterogeneous Catalysis: Recent Progress, New Trends, and Future Perspectives. *Chem Rev.* **2020,** *120*, 8468-8535.

(8)   Chen, H.; Liu, Y.; Cai, T.; Dong, W.; Tang, L.; Xia, X.; Wang, L.; Li, T., Boosting Photocatalytic Performance in Mixed-Valence MIL-53(Fe) by Changing Fe(II)/Fe(III) Ratio. *ACS Appl Mater Interfaces.* **2019,** *11*, 28791-28800.

(9)   Liu, N.; Huang, W.; Tang, M.; Yin, C.; Gao, B.; Li, Z.; Tang, L.; Lei, J.; Cui, L.; Zhang, X., In-Situ Fabrication of Needle-Shaped MIL-53(Fe) with 1T-MoS_2 and Study on Its Enhanced Photocatalytic Mechanism of Ibuprofen. *Chemical Engineering Journal.* **2019,** *359*, 254-264.

(10)   Hu, J.; Chen, D.; Mo, Z.; Li, N.; Xu, Q.; Li, H.; He, J.; Xu, H.; Lu, J., Z-Scheme 2D/2D Heterojunction of Black Phosphorus/Monolayer Bi_2WO_6 Nanosheets with Enhanced Photocatalytic Activities. *Angew Chem Int Ed Engl.* **2019,** *58*, 2073-2077.

(11)   Zhang, M.; Lu, M.; Lang, Z. L.; Liu, J.; Liu, M.; Chang, J. N.; Li, L. Y.; Shang, L. J.; Wang, M.; Li, S. L.; Lan, Y. Q., Semiconductor/Covalent-Organic-Framework Z-Scheme Heterojunctions for Artificial Photosynthesis. *Angew Chem Int Ed Engl.* **2020,** *59*, 6500-6506.

(12)   Cui, D.; Wang, L.; Du, Y.; Hao, W.; Chen, J., Photocatalytic Reduction on Bismuth-Based p-Block Semiconductors. *ACS Sustainable Chemistry & Engineering.* **2018,** *6*, 15936-15953.

(13)   Wang, H.; Yong, D.; Chen, S.; Jiang, S.; Zhang, X.; Shao, W.; Zhang, Q.; Yan, W.; Pan, B.; Xie, Y., Oxygen-Vacancy-Mediated Exciton Dissociation in BiOBr for Boosting Charge-Carrier-Involved Molecular Oxygen Activation. *J Am Chem Soc.* **2018,** *140*, 1760-1766.

(14)   Wang, Z.; Chen, M.; Huang, D.; Zeng, G.; Xu, P.; Zhou, C.; Lai, C.; Wang, H.; Cheng, M.; Wang, W., Multiply Structural Optimized Strategies for Bismuth Oxyhalide Photocatalysis and Their Environmental Application. *Chemical Engineering Journal.* **2019,** *374*, 1025-1045.

(15)   Wang, X.; Zhou, C.; Yin, L.; Zhang, R.; Liu, G., Iodine-Deficient BiOI Nanosheets with Lowered Valence Band Maximum To Enable Visible Light Photocatalytic Activity. *ACS Sustainable Chemistry & Engineering.* **2019,** *7*, 7900-7907.

(16)   Tian, N.; Huang, H.; Wang, S.; Zhang, T.; Du, X.; Zhang, Y., Facet-Charge-Induced Coupling Dependent Interfacial Photocharge Separation: A Case of BiOI/g-C$_3$N$_4$ p-n Junction. *Applied Catalysis B: Environmental.* **2020,** *267*, 118697.

(17)   Liu, F.; Shi, R.; Wang, Z.; Weng, Y.; Che, C. M.; Chen, Y., Direct Z-Scheme Hetero-Phase Junction of Black/Red Phosphorus for Photocatalytic Water Splitting. *Angew Chem Int Ed Engl.* **2019,** *58*, 11791-11795.

(18)   Chaturvedi, G.; Kaur, A.; Kansal, S. K., CdS-Decorated MIL-53(Fe) Microrods with Enhanced Visible Light Photocatalytic Performance for the Degradation of Ketorolac Tromethamine and Mechanism Insight. *The Journal of Physical Chemistry C.* **2019,** *123*, 16857-16867.

(19)   Xing, Z.; Hu, J.; Ma, M.; Lin, H.; An, Y.; Liu, Z.; Zhang, Y.; Li, J.; Yang, S., From One to Two: In Situ Construction of an Ultrathin 2D-2D Closely Bonded Heterojunction from a Single-Phase Monolayer Nanosheet. *J Am Chem Soc.* **2019,** *141*, 19715-19727.

(20)   Ma, R.; Zhang, S.; Li, L.; Gu, P.; Wen, T.; Khan, A.; Li, S.; Li, B.; Wang, S.; Wang, X., Enhanced Visible-Light-Induced Photoactivity of Type-II CeO$_2$/g-C$_3$N$_4$ Nanosheet toward Organic Pollutants Degradation. *ACS Sustainable Chemistry & Engineering.* **2019,** *7*, 9699-9708.

(21)   Xi, J.; Xia, H.; Ning, X.; Zhang, Z.; Liu, J.; Mu, Z.; Zhang, S.; Du, P.; Lu, X., Carbon-Intercalated 0D/2D Hybrid of Hematite Quantum Dots/Graphitic Carbon Nitride Nanosheets as Superior Catalyst for Advanced Oxidation. *Small.* **2019,** *15*, e1902744.

(22)   Ji, J.; Aleisa, R. M.; Duan, H.; Zhang, J.; Yin, Y.; Xing, M., Metallic Active Sites on MoO$_2$(110) Surface to Catalyze Advanced Oxidation Processes for Efficient Pollutant Removal. *iScience.* **2020,** *23*, 100861.

(23)   Yi, Q.; Ji, J.; Shen, B.; Dong, C.; Liu, J.; Zhang, J.; Xing, M., Singlet Oxygen Triggered by Superoxide Radicals in a Molybdenum Cocatalytic Fenton Reaction with Enhanced Redox Activity in the Environment. *Environ Sci Technol.* **2019,** *53*, 9725-9733.

(24)   Bui, V. K. H.; Park, D.; Pham, T. N.; An, Y.; Choi, J. S.; Lee, H. U.; Kwon, O. H.; Moon, J. Y.; Kim, K. T.; Lee, Y. C., Synthesis of MgAC-Fe$_3$O$_4$/TiO$_2$ Hybrid Nanocomposites via Sol-Gel Chemistry for Water Treatment by Photo-Fenton and Photocatalytic Reactions. *Sci Rep.* **2019,** *9*, 11855.

(25)   Liu, R.; Xu, Y.; Chen, B., Self-Assembled Nano-FeO(OH)/Reduced Graphene Oxide Aerogel as a Reusable Catalyst for Photo-Fenton Degradation of Phenolic Organics. *Environ Sci Technol.* **2018,** *52*, 7043-7053.

(26)   Liao, X.; Wang, F.; Wang, F.; Cai, Y.; Yao, Y.; Teng, B.-T.; Hao, Q.; Shuxiang, L., Synthesis of (100) Surface Oriented MIL-88A-Fe with Rod-Like Structure and Its Enhanced Fenton-Like Performance for Phenol Removal. *Applied Catalysis B: Environmental.* **2019,** *259*, 118064.

(27)   Wu, Q.; Yang, H.; Kang, L.; Gao, Z.; Ren, F., Fe-Based Metal-Organic Frameworks as Fenton-Like Catalysts for Highly Efficient Degradation of Tetracycline Hydrochloride over a Wide pH Range: Acceleration of Fe(II)/Fe(III) Cycle under Visible Light Irradiation. *Applied Catalysis B: Environmental.* **2020,** *263*, 118282.

(28)   Tong, W.; Xie, Y.; Luo, H.; Niu, J.; Ran, W.; Hu, W.; Wang, L.; Yao, C.; Liu, W.; Zhang, Y.; Wang, Y., Phosphorus-Rich Microorganism-Enabled Synthesis of Cobalt Phosphide/Carbon Composite for Bisphenol A Degradation through Activation of Peroxymonosulfate. *Chemical Engineering Journal.* **2019,** *378*, 122187.

(29)   Pan, F.; Ji, H.; Du, P.; Huang, T.; Wang, C.; Liu, W., Insights into Catalytic Activation of Peroxymonosulfate for Carbamazepine Degradation by MnO$_2$ Nanoparticles in-situ Anchored Titanate Nanotubes: Mechanism, Ecotoxicity and DFT study. *J Hazard Mater.* **2021,** *402*, 123779.

(30)   Hu, Z.; Cai, X.; Wang, Z.; Li, S.; Wang, Z.; Xie, X., Construction of Carbon-Doped Supramolecule-Based g-C$_3$N$_4$/TiO$_2$ Composites for Removal of Diclofenac and Carbamazepine: A Comparative Study of Operating Parameters, Mechanisms, Degradation Pathways. *J Hazard Mater.* **2019,** *380*, 120812.

(31)   Cui, J.; Pei, Y.; Hou, J.; Zheng, Y.; Zhang, Y.; Wei, K.; He, X.; Xi, B., Construction of A Carbon Dots-Based Z-scheme Photocatalytic Electrode with Enhanced Visible-Light-Driven Activity for

Cr(VI) Reduction and Carbamazepine Degradation in Different Reaction Systems. *Chemical Engineering Journal.* **2020,** 127571.

(32)   Trandafilović, L. V.; Jovanović, D. J.; Zhang, X.; Ptasińska, S.; Dramićanin, M. D., Enhanced Photocatalytic Degradation of Methylene Blue and Methyl Orange by ZnO:Eu Nanoparticles. *Applied Catalysis B: Environmental.* **2017,** *203*, 740-752.

(33)   Liu, D.; Chen, D.; Li, N.; Xu, Q.; Li, H.; He, J.; Lu, J., Surface Engineering of g-C_3N_4 by Stacked BiOBr Sheets Rich in Oxygen Vacancies for Boosting Photocatalytic Performance. *Angew Chem Int Ed Engl.* **2020,** *59*, 4519-4524.

(34)   Ge, G.; Liu, M.; Liu, C.; Zhou, W.; Wang, D.; Liu, L.; Ye, J., Ultrathin FeOOH Nanosheets as An Efficient Cocatalyst for Photocatalytic Water Oxidation. *Journal of Materials Chemistry A.* **2019,** *7*, 9222-9229.

(35)   He, X.; Fang, H.; Gosztola, D. J.; Jiang, Z.; Jena, P.; Wang, W. N., Mechanistic Insight into Photocatalytic Pathways of MIL-100(Fe)/TiO_2 Composites. *ACS Appl Mater Interfaces.* **2019,** *11*, 12516-12524.

(36)   Meng, J.; Niu, C.; Xu, L.; Li, J.; Liu, X.; Wang, X.; Wu, Y.; Xu, X.; Chen, W.; Li, Q.; Zhu, Z.; Zhao, D.; Mai, L., General Oriented Formation of Carbon Nanotubes from Metal-Organic Frameworks. *J Am Chem Soc.* **2017,** *139*, 8212-8221.

(37)   Osadchii, D. Y.; Olivos-Suarez, A. I.; Szécsényi, Á.; Li, G.; Nasalevich, M. A.; Dugulan, I. A.; Crespo, P. S.; Hensen, E. J. M.; Veber, S. L.; Fedin, M. V.; Sankar, G.; Pidko, E. A.; Gascon, J., Isolated Fe Sites in Metal Organic Frameworks Catalyze the Direct Conversion of Methane to Methanol. *ACS Catalysis.* **2018,** *8*, 5542-5548.

(38)   Li, X.; Wang, Z.; Zhang, B.; Rykov, A. I.; Ahmed, M. A.; Wang, J., $Fe_xCo_{3-x}O_4$ Nanocages Derived from Nanoscale Metal–Organic Frameworks for Removal of Bisphenol A by Activation of Peroxymonosulfate. *Applied Catalysis B: Environmental.* **2016,** *181*, 788-799.

(39)   Millange, F.; Guillou, N.; Walton, R. I.; Greneche, J. M.; Margiolaki, I.; Ferey, G., Effect of the Nature of the Metal on the Breathing Steps in MOFs with Dynamic Frameworks. *Chem Commun (Camb).* **2008,** *39*, 4732-4734.

(40)   Nosaka, Y.; Nosaka, A. Y., Generation and Detection of Reactive Oxygen Species in Photocatalysis. *Chem Rev.* **2017,** *117*, 11302-11336.

(41)   Huang, S.; Zhang, Q.; Liu, P.; Ma, S.; Xie, B.; Yang, K.; Zhao, Y., Novel Up-Conversion Carbon Quantum Dots/α-FeOOH Nanohybrids Eliminate Tetracycline and Its Related Drug Resistance in Visible-Light Responsive Fenton System. *Applied Catalysis B: Environmental.* **2020,** *263*, 118336.

(42)   Liu, D.; Chen, D.; Li, N.; Xu, Q.; Li, H.; He, J.; Lu, J., ZIF-67-Derived 3D Hollow Mesoporous Crystalline Co_3O_4 Wrapped by 2D g-C_3N_4 Nanosheets for Photocatalytic Removal of Nitric Oxide. *Small.* **2019,** *15*, e1902291.

(43)   Tang, M.; Ao, Y.; Wang, C.; Wang, P., Rationally Constructing of A Novel Dual Z-Scheme Composite Photocatalyst with Significantly Enhanced Performance for Neonicotinoid Degradation under Visible Light Irradiation. *Applied Catalysis B: Environmental.* **2020,** *270*, 118918.

(44)   Peng, B.; Lu, Y.; Luo, J.; Zhang, Z.; Zhu, X.; Tang, L.; Wang, L.; Deng, Y.; Ouyang, X.; Tan, J.; Wang, J., Visible Light-Activated Self-Powered Photoelectrochemical Aptasensor for Ultrasensitive Chloramphenicol Detection Based on DFT-Proved Z-Scheme Ag_2CrO_4/g-C_3N_4/Graphene Oxide. *Journal of Hazardous Materials.* **2021,** *401*, 123395.

(45)   Liang, C.; Feng, H.-P.; Niu, H.-Y.; Niu, C.-G.; Li, J.-S.; Huang, D.-W.; Zhang, L.; Guo, H.; Tang, N.; Liu, H.-Y., A Dual Transfer Strategy for Boosting Reactive Oxygen Species Generation in Ultrathin Z-Scheme Heterojunction Driven by Electronic Field. *Chemical Engineering Journal* **2020,** *384*, 123236.

(46)   Zhou, L.; Lei, J.; Wang, L.; Liu, Y.; Zhang, J., Highly Efficient Photo-Fenton Degradation of Methyl Orange Facilitated by Slow Light Effect and Hierarchical Porous Structure of Fe_2O_3-SiO_2 Photonic Crystals. *Applied Catalysis B: Environmental.* **2018,** *237*, 1160-1167.

(47)   Dou, X.; Zhang, Q.; Shah, S. N. A.; Khan, M.; Uchiyama, K.; Lin, J.-M., MoS_2-Quantum Dot Triggered Reactive Oxygen Species Generation and Depletion: Responsible for Enhanced Chemiluminescence. *Chemical Science*. **2019**, *10*, 497-500.

(48)   Su, Y.; Wu, Z.; Wu, Y.; Yu, J.; Sun, L.; Lin, C., Acid Orange II Degradation Through A Heterogeneous Fenton-Like Reaction Using Fe–TiO_2 Nanotube Arrays as A Photocatalyst. *Journal of Materials Chemistry A*. **2015**, *3*, 8537-8544.

(49)   Xing, M.; Xu, W.; Dong, C.; Bai, Y.; Zeng, J.; Zhou, Y.; Zhang, J.; Yin, Y., Metal Sulfides as Excellent Co-catalysts for H_2O_2 Decomposition in Advanced Oxidation Processes. *Chem*. **2018**, *4*, 1359-1372.

(50)   Hu, J.; Li, J.; Cui, J.; An, W.; Liu, L.; Liang, Y.; Cui, W., Surface Oxygen Vacancies Enriched FeOOH/Bi_2MoO_6 Photocatalysis-Fenton Synergy Degradation of Organic Pollutants. *Journal of Hazardous Materials*. **2020**, *384*, 121399.

(51)   Cheng, D.; Liao, W.; Yuan, S., Effect of in Situ Generated Iron Oxyhydroxide Coatings on FeS Oxygenation and Resultant Hydroxyl Radical Production for Contaminant Degradation. *Chemical Engineering Journal*. **2020**, *394*, 124961.

(52)   Li, X.; Cui, K.; Guo, Z.; Yang, T.; Cao, Y.; Xiang, Y.; Chen, H.; Xi, M., Heterogeneous Fenton-Like Degradation of Tetracyclines Using Porous Magnetic Chitosan Microspheres as An Efficient Catalyst Compared with Two Preparation Methods. *Chemical Engineering Journal*. **2020**, *379*, 122324.

(53)   Wei, Y.; Yu, X.; Liu, C.; Ma, J.; Wei, S.; Chen, T.; Yin, K.; Liu, H.; Luo, S., Enhanced Arsenite Removal from Water by Radially Porous Fe-Chitosan Beads: Adsorption and H_2O_2 Catalytic Oxidation. *J Hazard Mater*. **2019**, *373*, 97-105.

(54)   Chagas, P. M. B.; Caetano, A. A.; Tireli, A. A.; Cesar, P. H. S.; Correa, A. D.; Guimaraes, I. D. R., Use of an Environmental Pollutant From Hexavalent Chromium Removal as a Green Catalyst in The Fenton Process. *Sci Rep*. **2019,** *9*, 12819.

Table of Content